

# FREQUENCY-TUNED ACM FOR BIOMEDICAL IMAGE SEGMENTATION

*Qing Guo<sup>1,2</sup>, Shuifa Sun<sup>2,†</sup>, Fangmin Dong<sup>2</sup>, Wei Feng<sup>1</sup>, Bruce Zhi Gao<sup>3</sup>, and Siyu Ma<sup>3</sup>*

<sup>1</sup> School of Computer Science and Technology, Tianjin University, Tianjin, China

<sup>2</sup> College of Computer and Information Technology, China Three Gorges University, Hubei, China

<sup>3</sup> Department of Bioengineering, COMSET, Clemson University, Clemson SC, USA

## ABSTRACT

Biomedical images are usually corrupted by strong noise and intensity inhomogeneity simultaneously. Existing region-based active contour models (RACMs) easily fail when segmenting such images. In the frequency domain, we propose a generalized RACM that presents a new way to understand the essence of classical RACMs whose segmentation results are determined by a frequency filter to extract the proposed frequency boundary energy. Then, we introduce the difference of Gaussians as the optimal filter to exclude strong noise and intensity inhomogeneity effectively. We show superior performance of the model by comparing with six state-of-the-art methods on challenge biomedical images and segmenting an optical coherence tomography image sequence.

**Index Terms**— biomedical image segmentation, active contour model, frequency boundary energy

## 1. INTRODUCTION

Active contour models (ACMs) [1, 2] can obtain sub-pixel precision segmentation and smooth contours, and are widely employed in medical image segmentation. ACMs are mainly classified into two types: edge-based [2–7] and region-based ACMs (RACMs) [1,8–21]. RACMs can handle various noise and weak edges usually found in medical images.

Let an image  $\mathbf{I}$  be  $\Omega \rightarrow \mathbb{R}$  with  $\Omega$  being the image domain  $\mathbb{R}^2$  and contain an object whose boundary is denoted as  $C$ . A contour  $C_t$  is first initialized on the image and partitions  $\mathbf{I}$  into sub-regions outside and inside the  $C_t$  ( $\Omega_1$  and  $\Omega_2$ ). Then, RACMs restrain  $C_t$  to  $C$  via minimizing an energy function based on region features and get segmentation with sub-regions being object and background [1, 9, 19]. The Mumford-Shah model [8] laid the foundation for RACMs. However, it is very difficult to converge to the optimal solution for the non-convexity of its energy function. Then, Chan-

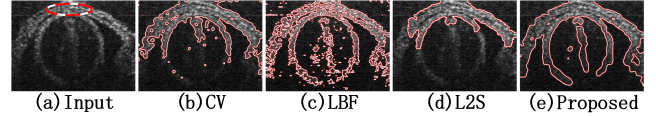


**Fig. 1.** Segmenting optical coherence tomography (OCT) image with CV [9, 10], LBF [12, 13], legendre level set (L2S) [22] and our method. The dashed line in (a) is the initial contour for all methods.

Vese (CV) model [9] was developed and defined as

$$E^{CV}(C_t, a_i) = \sum_{i=1}^2 \int_{\Omega_i} |\mathbf{I}(\mathbf{x}) - a_i|^2 d\mathbf{x}, \quad (1)$$

where  $\mathbf{x} \in \Omega$  is the coordinate vector.  $a_i$  is the average intensity of  $\Omega_i$  and can be regarded as global region information which helps CV to segment homogeneous images effectively. However, it fails to handle intensity inhomogeneity, e.g. Fig. 1 (b). To overcome this problem, local binary fitting (LBF) model [12, 13] is proposed and defined as

$$E^{LBF}(C_t, \mathbf{f}_i(\mathbf{x})) = \int_{\Omega} \varepsilon_{\mathbf{x}}^{\text{Fit}}(C_t, \mathbf{f}_1(\mathbf{x}), \mathbf{f}_2(\mathbf{x})) d\mathbf{x}, \quad (2)$$

where  $\varepsilon_{\mathbf{x}}^{\text{Fit}}$  encourages local smooth via Gaussian function, i.e.  $K(\cdot)$ , with  $\mathbf{y}$  being the neighbor of  $\mathbf{x}$  and is defined as

$$\varepsilon_{\mathbf{x}}^{\text{Fit}}(C_t, \mathbf{f}_i(\mathbf{x})) = \sum_{i=1}^2 \int_{\Omega_i} K(\mathbf{x} - \mathbf{y}) |\mathbf{I}(\mathbf{y}) - \mathbf{f}_i(\mathbf{x})|^2 d\mathbf{y}, \quad (3)$$

where  $\mathbf{f}_i(\mathbf{x})$  is the gaussian weight summation of the neighborhood of  $\mathbf{x}$ . Similarly, another local region based ACM, i.e. local image fitting (LIF) model [11] is defined as

$$E^{LIF}(C_t, \mathbf{f}_i(\mathbf{x})) = \sum_{i=1}^2 \int_{\Omega_i} |\mathbf{I}(\mathbf{x}) - \mathbf{f}_i(\mathbf{x})|^2 d\mathbf{x}. \quad (4)$$

With local region information, LBF and LIF can segment images with intensity inhomogeneity. However, they are sensitive to strong noise, e.g. Fig. 1 (c). Therefore, classical RACMs fail to segment images with strong noise and intensity inhomogeneity simultaneously.

However, many biomedical images are corrupted by strong noise and intensity inhomogeneity simultaneously because of the limitations in imaging technology. For example, the optical coherence tomography (OCT) heart tube

<sup>†</sup> is corresponding author. Email: watersun1977@hotmail.com. This paper is supported by Natural Science Foundation of China (No.61272237, No.61272236, No.61273243), Hubei Natural Science Fund for Innovative Research Groups (No.2015CFA025)

images shown in Fig. 1 are corrupted by strong speckle noise and bias. Global or local RACMs fail to obtain smooth segmentation. Recently, many improved RACMs were proposed via effectively utilizing image information [14, 17, 19, 22] or improving the method of minimizing the energy function [10, 18]. For example, [22] proposed legendre level set (L2S), which represents region information as a set of Legendre basis functions and is able to handle noise and intensity inhomogeneity. These models achieve better results in some cases, but they still have limitations when segmenting complex images, *e.g.* Fig. 1 (b)-(d).

In this paper, we propose a generalized RACM by defining frequency boundary energy (FBE) in the frequency domain. Image segmentation is defined as finding a contour that minimizes the FBE outside and inside the contour. Thus, the segmentation result is decided by a frequency filter that produces FBE. Then, we introduce two frequency filters being demonstrated to be classical RACMs, which indicates that FBE is a generalized RACM. Finally, we propose to use difference of Gaussians as a better filter to exclude strong noise and intensity inhomogeneity effectively. Extensive experiments demonstrate the proposed model achieves better results than six state-of-the-art methods.

## 2. THE METHOD

### 2.1. Frequency boundary energy

$C$  is the boundary between the object and the background. The goal of ACM is to restrain  $C_t$  to  $C$  and gets segmentation. In the frequency domain, the fourier transform of an image  $\mathbf{I}$  is  $\mathbf{S} = \Im(\mathbf{I}, \Omega)$ , with its power spectrum being  $\mathbf{P}(\mathbf{u}) = |\mathbf{S}(\mathbf{u})|^2$ , where  $\mathbf{u}$  is the coordinate vector in frequency domain. Here, we focus on the energy of the object boundary  $C$  in sub-regions ( $\Omega_1$  and  $\Omega_2$ ) divided by  $C_t$  and define  $\mathbf{P}_i$  as the power spectra of  $C$  in  $\Omega_i$ . Thus, the energy of  $C$  contained in  $\Omega/C_t$  is presented as

$$E^{FBE}(C_t) = \sum_{i=1}^2 \int_{\Im(\mathbf{I}, \Omega_i)} \mathbf{P}_i(\mathbf{u}) d\mathbf{u}. \quad (5)$$

Clearly, when Eq. (5) is minimized, *i.e.* the energy of  $C$  in both subregions vanishes,  $C$  is not included in any subregions, *i.e.*  $C_t$  equals to  $C$  with segmentation being obtained. Fig. 2 shows an example in which  $C_t$  gradually fits to  $C$  with the reducing of  $E^{FBE}$ . We denote Eq. (5) as frequency boundary energy (FBE). The key of using FBE is to define  $\mathbf{P}_i$ . As  $\mathbf{P}_i$  represents the energy of  $C$ , we can use a frequency filter ( $\mathbf{F}(\mathbf{u})$ ) to extract the  $C$  in the frequency domain for sub-region  $\Omega_i$ , *i.e.*  $\mathbf{S}_i(\mathbf{u})\mathbf{F}(\mathbf{u})$  with  $\mathbf{S}_i(\mathbf{u})$  being the fourier transform of sub-region  $\Omega_i$ . Thus, FBE can be rewritten as

$$E^{FBE}(C_t) = \sum_{i=1}^2 \int_{\Im(\mathbf{I}, \Omega_i)} |\mathbf{S}_i(\mathbf{u})\mathbf{F}(\mathbf{u})|^2 d\mathbf{u}. \quad (6)$$

However, we cannot calculate the fourier transform of  $\Omega_i$  directly due to their arbitrary shapes, which limits the appli-

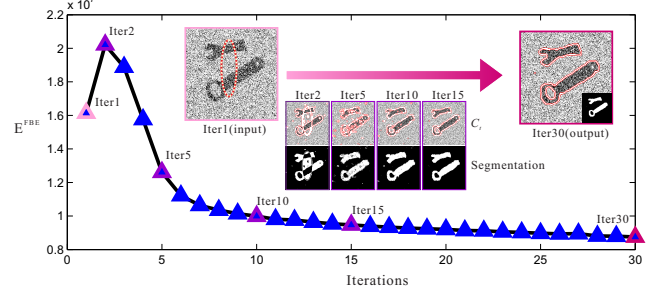


**Fig. 2.** An example of minimizing FBE. As  $E^{FBE}$  reducing, the energy of  $C$  in subregions gradually vanishes. Finally,  $C_t$  is restricted to  $C$  with segmentation result obtained.

cation of FBE. Fortunately, with the level set  $\phi$  representation of  $C_t$  and the Heaviside function  $H(\cdot)$  detailed in [9], we can represent each sub-region  $\Omega_i$  as  $M_i(\phi)\mathbf{I}$  with  $M_1(\phi) = H(\phi)$  and  $M_2(\phi) = 1 - H(\phi)$ . Thus, the fourier transform of  $\Omega_i$  can be approximated as  $\hat{\mathbf{S}}_i(\mathbf{u}) = \Im(M_i(\phi)\mathbf{I}, \Omega)$ . Since  $M_i(\phi)$  also introduces energy into  $\hat{\mathbf{S}}_i(\mathbf{u})$ , we should regularize it in spatial domain and rewrite Eq. (6) as

$$E^{FBE}(\phi) = \sum_{i=1}^2 \int_{\Im(M_i(\phi)\mathbf{I}, \Omega)} \left| \frac{\Im^{-1}(\hat{\mathbf{S}}_i(\mathbf{u})\mathbf{F}(\mathbf{u}))}{\Im^{-1}(\Im(M_i(\phi))\mathbf{F}(\mathbf{u}))} \right|^2 d\mathbf{u}. \quad (7)$$

Theoretically, as long as  $\mathbf{F}(\mathbf{u})$  is able to accurately extract boundary information, the segmentation result is optimized when the FBE is minimized. Thus, selection of  $\mathbf{F}(\mathbf{u})$  is key to achieving effective segmentation.

### 2.2. $\mathbf{F}(\mathbf{u})$ designing

We first introduce the two  $\mathbf{F}(\mathbf{u})$  and demonstrate their relation to classical models, which shows that FBE model is a generalized RACM. Then, we propose the difference of Gaussians as a better filter to segment images with both strong noise and intensity inhomogeneity.

#### 2.2.1. Ideal high-pass filter

We set  $\mathbf{F}(\mathbf{u})$  as an ideal high-pass filter,

$$\mathbf{F}(\mathbf{u}) = 1 - \mathbf{F}_{Ilp}(\mathbf{u}), \quad \mathbf{F}_{Ilp}(\mathbf{u}) = \begin{cases} 0, & \mathbf{u} \neq (0, 0) \\ 1, & \mathbf{u} = (0, 0) \end{cases}. \quad (8)$$

Due to energy conservation of fourier transform, We can rewrite the Eq.(6) in spatial domain,

$$E^{FBE}(C_t) = \sum_{i=1}^2 \int_{\Omega_i} |\mathbf{I}(\mathbf{x}) - \mathbf{I} * \mathbf{f}_{Ilp}|^2 d\mathbf{x}, \quad (9)$$

where  $\mathbf{f}_{Ilp}$  is the spatial filter of  $\mathbf{F}_{Ilp}$ ;  $*$  denotes the convolution operation. Since convoluting the  $\Omega_i$  with ideal low-pass filter equals to calculate the average value of  $\Omega_i$ , *i.e.*  $a_i$ , Eq. (9) can be rewritten as

$$E^{FBE}(C_t) = \sum_{i=1}^2 \int_{\Omega_i} |\mathbf{I}(\mathbf{x}) - a_i|^2 d\mathbf{x}. \quad (10)$$

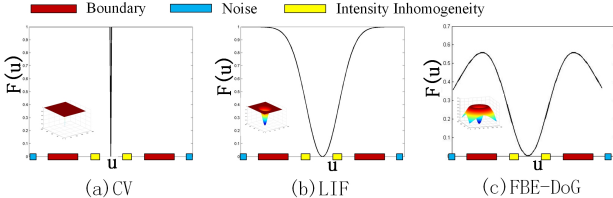


**Fig. 3.** Three  $\mathbf{F}(\mathbf{u})$  corresponding to CV, LIF and FBE-DoG. The color squares on horizontal axis represent the possible information distribution of a image.

Obviously, Eq. (10) is consistent with Eq. (1). Therefore, CV is a specific form of FBE model when  $\mathbf{F}(\mathbf{u})$  is set as an ideal high-pass filter. Furthermore, as shown in Fig. 3 (a), with  $\mathbf{F}(\mathbf{u})$  being ideal high-pass filter, the FBE contains both boundary and other interference, e.g. strong noise and intensity inhomogeneity, which leads the CV model is easily affected by noise and intensity inhomogeneity.

### 2.2.2. Gaussian high-pass filter

We then set  $\mathbf{F}(\mathbf{u})$  being the Gaussian high-pass filter,

$$\mathbf{F}(\mathbf{u}) = 1 - \mathbf{F}_{\text{Glp}}(\mathbf{u}), \mathbf{F}_{\text{Glp}}(\mathbf{u}) = \exp\left(-\frac{D^2(\mathbf{u})}{2D_0^2}\right), \quad (11)$$

where  $D(\mathbf{u})$  represents the distance from point  $\mathbf{u}$  to the zero frequency.  $D_0$  is the cutoff frequency.  $\mathbf{f}_{\text{Glp}}(\mathbf{x})$  is the spatial filter of  $\mathbf{F}_{\text{Glp}}(\mathbf{u})$ . Thus, Eq. (6) can be rewritten as

$$E^{\text{FBE}}(C_t) = \sum_{i=1}^2 \int_{\Omega_i} |\mathbf{I}(\mathbf{x}) - \mathbf{f}_i(\mathbf{x})|^2 d\mathbf{x}, \quad (12)$$

where  $\mathbf{f}_i(\mathbf{x}) = (I, \Omega_i) * \mathbf{f}_{\text{Glp}}$ . Therefore, Eq. (12) is consistent with Eq. (4), and LIF is a specific form of FBE model, with  $\mathbf{F}(\mathbf{u})$  being the Gaussian high-pass filter. As shown in Fig. 3 (b), the Gaussian high-pass filter helps to limit the intensity inhomogeneity which is a low frequency component. However, the noise is still included in the  $E^{\text{FBE}}$  which make LIF fail to handle images with strong noise.

Furthermore, we rewrite Eq. (3) as a discrete form:

$$\varepsilon_{\mathbf{x}}^{\text{Fit}} = \sum_{i=1}^2 \sum_{j=1}^M w_j |\mathbf{I}(\mathbf{y}_j) - \mathbf{f}_i(\mathbf{x})|^2, \quad (13)$$

where  $w_j$  is the coefficient of the Gaussian kernel with  $0 < w_j < 1$ .  $M$  is the size of the Gaussian kernel. Therefore, Eq. (2) can be rewritten as Eq. (14).

$$\begin{aligned} E^{\text{LBF}} &= \sum_{j=1}^M w_j \sum_{i=1}^2 \int_{\Omega_i} |\mathbf{I}(\mathbf{y}_j) - \mathbf{f}_i(\mathbf{x})|^2 d\mathbf{x} \\ &= w_1 E^{\text{LIF}} + \sum_{j=2}^M w_j \hat{E}^{\text{LIF}}. \end{aligned} \quad (14)$$

We assume  $\mathbf{I}(\mathbf{y}_i) \approx \mathbf{I}(\mathbf{x})(i \neq 1)$ ; the degree of approximation is determined by  $w_j$ . Thus,  $E^{\text{LBF}}$  equals a weighted combination of  $E^{\text{LIF}}$  and its approximations. This explains why LIFM can obtain results similar to those of LBF [11].

### 2.2.3. DoG filter

We have shown that the classical RACMs are the special cases of our FBE model by setting ideal or gaussian high-pass filter as the  $\mathbf{F}(\mathbf{u})$  and cannot handle strong noise and intensity inhomogeneity simultaneously. To get better segmentation, we propose to set  $\mathbf{F}(\mathbf{u})$  being a band-pass filter to limit both high and low frequency interferences. Obviously, the DoG shown in Fig. 3 (c) is suitable, being widely used in edge extraction, feature point detection [23] and salient region detection [24]. Then, we set  $\mathbf{F}(\mathbf{u})$  being the DoG filter, i.e.

$$\mathbf{F}(\mathbf{u}) = \text{DoG}(\mathbf{u}) = G(\mathbf{u}, \sigma_1) - G(\mathbf{u}, \sigma_2), \quad (15)$$

$$G(\mathbf{u}, \sigma_i) = \frac{1}{2\pi\sigma_i^2} \exp\left(-\frac{\mathbf{u}^T \mathbf{u}}{2\sigma_i^2}\right). \quad (16)$$

Substituting Eq. (15) into Eq. (6), the FBE-DoG is obtained. The bandwidth and position of the DoG filter are determined by the values and ratio of  $\sigma_1$  and  $\sigma_2$ . Therefore, by selecting the correct  $\sigma_i$  for different images, FBE-DoG can obtain the better segmentation result.

## 2.3. Optimization

We combine Eq. (7) with the length and level set regularization term defined in [5, 11]. With the gradient descent algorithm, the minimization of Eq. (7) w.r.t  $\phi$  is defined as

$$\begin{aligned} \frac{\partial \phi}{\partial t} &= \lambda [\mathbf{f}_{b2}^2(\mathbf{x}) - \mathbf{f}_{b1}^2(\mathbf{x})] \delta(\phi) \\ &+ \mu (\nabla^2 \phi - \text{div}(\frac{\nabla \phi}{|\nabla \phi|})) + \nu \delta(\phi) \text{div}(\frac{\nabla \phi}{|\nabla \phi|}), \end{aligned} \quad (17)$$

Where  $\lambda$ ,  $\mu$  and  $\nu$  are the weighted factors for three terms;  $\delta(\cdot)$  is the Dirac delta function;  $\mathbf{f}_{bi}(\mathbf{x})$  is defined as

$$\mathbf{f}_{bi}(\mathbf{x}) = \frac{\Im^{-1}(\hat{\mathbf{S}}_i(\mathbf{u}) \mathbf{F}(\mathbf{u}))}{\Im^{-1}(\Im(M_i(\phi)) \mathbf{F}(\mathbf{u}))}. \quad (18)$$

## 3. EXPERIMENTS

### 3.1. Setup

We use the DRIVE dataset [25] that contains 40 noiseless retinal images to evaluate the performance of our method. These images are seriously corrupted by intensity inhomogeneity as shown in the first row of Fig. 4. Furthermore, we extend a noise version by add serious additive Gaussian noise to DRIVE dataset to evaluate the ability of handling strong noise and intensity inhomogeneity simultaneously. Besides, we also use our method to segment optical coherence heart image sequences to show its practicability. We use the CREASEG platform [26] to compare our method with six RACMs, i.e. b-spline level-set (BSLS) [10], selective local or global segmentation [18], local region ACM (LRACM) [20], local gaussian distribution fitting energy (LGDF) [17], local binary fitting (LBF) [13] and recent method level set with legendre

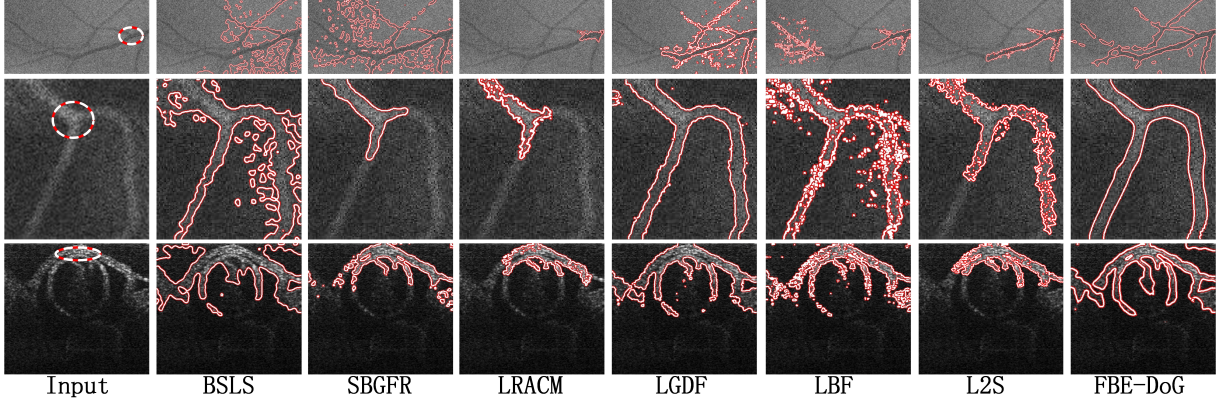


**Fig. 4.** Comparing with six ACM methods. The first image is one of the results in DRIVE Dataset; the second images are corrupted by strong multiplicative noise; the third image is the original OCT image corrupted by both speckle noise and intensity inhomogeneity.

**Table 1.** Average DICE and PSNR of Segmenting the DRIVE Dataset and Its Noisy Version.

Method	noiseless images		noisy images	
	DICE	PSNR	DICE	PSNR
BSLS [10]	0.24	3.39	0.27	4.13
SBGFR [18]	0.38	4.05	0.38	4.24
LRACM [20]	0.07	8.03	0.08	8.06
LGDF [17]	0.71	10.78	0.51	8.87
LBF [12]	0.74	11.42	0.29	8.13
L2S [22]	0.63	29.90	0.27	7.14
<b>FBE-DoG</b>	<b>0.78</b>	<b>11.99</b>	<b>0.62</b>	<b>9.42</b>

polynomials (L2S) [22]. The DICE and PSNR used in [25] work as the metrics to evaluate the segmentation accuracy.

Three parameters of our method in Eq. (17) are fixed for all experiments and set as:  $\lambda = 1$ ,  $\mu = 0.1$  and  $\nu = 0.009$ . The  $\sigma_1$  and  $\sigma_2$  used in Eq. (15) are fixed for different datasets. Specifically, for DRIVE dataset, we set  $\sigma_1 = 0.4$  and  $\sigma_2 = 0.01$ ; for OCT images, we set  $\sigma_1 = 0.5$  and  $\sigma_2 = 0.02$ .

### 3.2. Comparing with state-of-the-art methods

Comparison results on both noiseless and noise version of DRIVEN dataset are summarized in Table 1. Our method achieves best performance comparing with six baselines on both DICE and PSNR. On noiseless version, FBE-DoG gets 0.78 and 11.99 on DICE and PSNR, respectively, followed by LBF and LGDF. On noise version, the values of both metrics of our method are reduced to 0.62 and 9.42, respectively. However, the performance of LBF decreases significantly on the noise version, which indicates the LBF cannot handle strong noise properly, since it does not limit the high frequency introduced by noise as presented in subsection 2.2.2. We also show the segmentation results of seven methods in Fig. 4. Obviously, our method achieves the best segmentation accuracy with smooth contour for noisy DRIVEN image (the first row), blood image (second row) corrupted by multiplicative noise and real OCT image (third row).

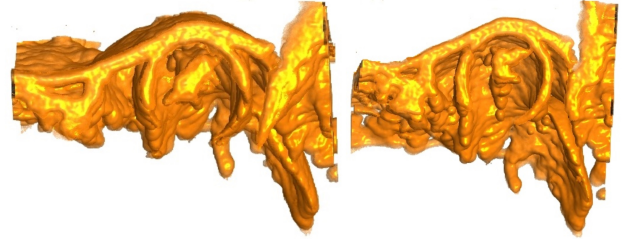


**Fig. 5.** 3D model constructed from OCT image sequence segmentation results.

### 3.3. Application to segment OCT image sequence

With FBE-DoG, we segment an OCT image sequence obtained from an embryonic chick heart tube to reconstruct a 3D model to understand the mechanism of formation of the avian heart. These images are corrupted by both strong noise and intensity inhomogeneity [27]. The initial contour is selected manually to segment the first image of the sequence. Thereafter, the result of segmentation of the prior image is used as the initial contour for the next image. A 3D model is made based on the segmentation results, as shown in Fig. 5. This application shows that the FBE-DoG model overcomes the influence of noise and intensity inhomogeneity in medical images and extracts the main information (*e.g.* the heart tube).

## 4. CONCLUSION

We have proposed a generalized region-based ACM in frequency domain by defining a frequency boundary energy (F-BE). We use DoG filter to extract the FBE, which can segment images with strong noise and intensity inhomogeneity. Extensive experiments on retinal and OCT heart tube images show that our method gets higher segmentation accuracy and smoother contour than six state-of-the-art methods. We also show that classical RACMs are special cases of FBE model via setting different frequency filters. In the future, we will extend the model to include more discriminative feature such as color, texture and priors to obtain better results. We will also attempt to learn the parameters on large dataset.

## 5. REFERENCES

- [1] D. Cremers, M. Rousson, and R. Deriche, “A review of statistical approaches to level set segmentation: integrating color, texture, motion and shape,” *Int. J. Comput. Vis.*, vol. 72, no. 2, pp. 195–215, 2007.
- [2] M. Kass, A. Witkin, and D. Terzopoulos, “Snakes: Active contour models,” *Int. J. Comput. Vis.*, vol. 1, no. 4, pp. 321–331, 1988.
- [3] V. Caselles, R. Kimmel, and G. Sapiro, “Geodesic active contours,” *Int. J. Comput. Vis.*, vol. 22, no. 1, pp. 61–79, 1997.
- [4] C. Xu and J.-L. Prince, “Snakes, shapes, and gradient vector flow,” *IEEE Trans. Image Process.*, vol. 7, no. 3, pp. 359–369, 1998.
- [5] C. Li, C. Xu, C. Gui, and M.D. Fox, “Level set evolution without re-initialization: a new variational formulation,” in *IEEE Conf. Computer Vision and Pattern Recognition (CVPR)*, 2005, pp. 430–436.
- [6] H. Benninghoff and H. Garcke, “Image segmentation using parametric contours with free endpoints,” *IEEE Trans. Image Process.*, vol. 25, no. 4, pp. 1639–1648, 2016.
- [7] A. Pratondo, C. K. Chui, and S. H. Ong, “Robust edge-stop functions for edge-based active contour models in medical image segmentation,” *IEEE Signal Process. Lett.*, vol. 23, no. 2, pp. 222–226, 2016.
- [8] D. Mumford and J. Shah, “Optimal approximations by piecewise smooth functions and associated variational problems,” *Commun. Pure Appl. Math.*, vol. 42, no. 5, pp. 577–685, 1989.
- [9] T.F. Chan and L.A. Vese, “Active contours without edges,” *IEEE Trans. Image Process.*, vol. 10, no. 2, pp. 266–277, 2001.
- [10] O. Bernard, D. Friboulet, P. Thevenaz, and M. Unser, “Variational b-spline level-set: A linear filtering approach for fast deformable model evolution,” *IEEE Trans. Image Process.*, vol. 18, no. 6, pp. 1179–1191, 2009.
- [11] K. Zhang, H. Song, and L. Zhang, “Active contours driven by local image fitting energy,” *Pattern Recogn.*, vol. 43, no. 4, pp. 1199 – 1206, 2010.
- [12] C. Li, C.-Y. Kao, J.-C. Gore, and Z. Ding, “Implicit active contours driven by local binary fitting energy,” in *IEEE Conf. Computer Vision and Pattern Recognition (CVPR)*, 2007, pp. 1–7.
- [13] C. Li, C.-Y. Kao, J.C. Gore, and Z. Ding, “Minimization of region-scalable fitting energy for image segmentation,” *IEEE Trans. Image Process.*, vol. 17, no. 10, pp. 1940–1949, 2008.
- [14] Y. Wang, S. Xiang, C. Pan, L. Wang, and G. Meng, “Level set evolution with locally linear classification for image segmentation,” *Pattern Recogn.*, vol. 46, no. 6, pp. 1734 – 1746, 2013.
- [15] D. Lui, C. Scharfenberger, K. Fergani, A. Wong, and D.A. Clausi, “Enhanced decoupled active contour using structural and textural variation energy functionals,” *IEEE Trans. Image Process.*, vol. 23, no. 2, pp. 855–869, Feb 2014.
- [16] N. Paragios and R. Deriche, “Geodesic active regions and level set methods for supervised texture segmentation,” *Int. J. Comput. Vis.*, vol. 46, no. 3, pp. 223–247, 2002.
- [17] L. Wang, L. He, A. Mishra, and C. Li, “Active contours driven by local gaussian distribution fitting energy,” *Signal Process.*, vol. 89, no. 12, pp. 2435 – 2447, 2009.
- [18] K. Zhang, L. Zhang, H. Song, and W. Zhou, “Active contours with selective local or global segmentation: A new formulation and level set method,” *Image Vision Comput.*, vol. 28, no. 4, pp. 668 – 676, 2010.
- [19] H. Wu, V. Appia, and A. Yezzi, “Numerical conditioning problems and solutions for nonparametric i.i.d. statistical active contours,” *IEEE Trans. Pattern Anal. Mach. Intell.*, vol. 35, no. 6, pp. 1298–1311, 2013.
- [20] S. Lankton and A. Tannenbaum, “Localizing region-based active contours,” *IEEE Trans. Image Process.*, vol. 17, no. 11, pp. 2029–2039, 2008.
- [21] L. Wang and C. Pan, “Explicit order model for region-based level set segmentation,” in *ICASSP*, 2015, pp. 927–931.
- [22] S. Mukherjee and S.-T. Acton, “Region based segmentation in presence of intensity inhomogeneity using legendre polynomials,” *IEEE Signal Process. Lett.*, vol. 22, no. 3, pp. 298–302, March 2015.
- [23] D.-G. Lowe, “Distinctive image features from scale-invariant keypoints,” *Int. J. Comput. Vis.*, vol. 60, no. 2, pp. 91–110, 2004.
- [24] R. Achanta, S. Hemami, F. Estrada, and S. Susstrunk, “Frequency-tuned salient region detection,” in *IEEE Conf. Computer Vision and Pattern Recognition (CVPR)*, 2009, pp. 1597–1604.
- [25] J. Staal, M.D. Abramoff, M. Niemeijer, M.A. Viergever, and B. van Ginneken, “Ridge-based vessel segmentation in color images of the retina,” *IEEE Trans. Med. Imag.*, vol. 23, no. 4, pp. 501–509, 2004.
- [26] T. Dietenbeck, M. Alessandrini, D. Friboulet, and O. Bernard, “Creaseg: A free software for the evaluation of image segmentation algorithms based on level-set,” in *IEEE Int. Conf. Image Processing*, 2010, pp. 665–668.
- [27] R. Wang, J.-X. Yun, R. Goodwin, R. Markwald, T.-K. Borg, R.-B. Runyan, and B. Gao, “4d imaging of embryonic chick hearts by streak-mode fourier domain optical coherence tomography,” *Proc. SPIE*, vol. 8207, pp. 82073V–82073V–6, 2012.